INTERNATIONAL JOURNAL FOR NUMERICAL METHODS IN FLUIDS
Int. J. Numer. Meth. Fluids 2002; **39**:719–741 (DOI: 10.1002/fld.347)

A low-dimensional spectral approach for transient free-surface flow inside thin cavities of symmetric shape

Sheng X. Zhang and Roger E. Khayat*,†

Department of Mechanical and Materials Engineering, The University of Western Ontario, London, Ont., Canada N6A 5B9

SUMMARY

The lubrication theory is extended for transient free-surface flow of a viscous fluid inside three-dimensional cavities of general symmetric shape but of small thickness. The problem is closely related to the filling stage during the injection molding process. The moving domain is mapped onto a rectangular domain at each time step of the computation. A modified pressure is introduced, which in this case is governed by the Laplace's equation, and it is expanded in a Fourier series along the flow direction. The expansion coefficients are obtained using the finite-difference method. This approach is valid for simple and complex cavities as illustrated for the cases of a flat plate and a curved plate. Only a few modes are needed to secure convergence in general. It is found that the flow behaviour is strongly influenced by the shape of the initial fluid domain, the shape of the cavity, cavity thickness, and the inlet flow. Copyright © 2002 John Wiley & Sons, Ltd.

1. INTRODUCTION

The modelling and simulation of free-surface cavity flow have been the object of considerable interest over the last two decades. The interest in this area of research activity is largely due to the need for new computational algorithms that assist in the design and fabrication of plastic and metal parts as encountered in the processing industry, particularly in injection molding and die casting. Modelling of the flow in these processes represent several major challenges since it is inherently transient, non-isothermal, and includes a free surface moving through cavities of highly irregular geometry. Despite the continuous development of new solution techniques, and the advent of powerful computational platforms, the simulation of free-surface flow inside a cavity remains challenging. For transient free-surface flow, the presence of geometrical non-linearities, coupled to material non-linearities, such as inertia (die casting) and non-Newtonian (injection molding) effects, make the moving-domain problem difficult to solve and understand.

*Correspondence to: R. E. Khayat, Department of Mechanical and Materials Engineering, Faculty of Engineering Science, The University of Western Ontario, London, Ont., Canada N6A 5B9.
†E-mail: rkhayat@eng.uwo.ca

Contract/grant sponsor: National Sciences and Engineering Council.

Received January 2001
Revised November 2001

Due to limited computational resources, the three-dimensional flow problem has customarily been simplified to a two-dimensional problem, based on the observation of Hele-Shaw [1–3]. The method is closely related to the lubrication or shallow-water theory for Newtonian flow [4]. In this approach, the cavity is assumed to be thin, and out of plane flows are neglected. Richardson [5] was the first to propose this method for molding flow. He examined Newtonian, isothermal flow inside cavities of simple geometry. Three decades later, the lubrication assumption remains the basis for the simulation of free-surface flow of thin films [6–8]. Various flow configurations were analyzed: Kamal and Kenig [9], Winter [10], and Berger and Gogos [11] have examined the case of radial flow from a central injection point. White [12], Broyer et al. [13], and Van Wijngaarden et al. [14], among others, have analysed the flow between parallel and non-parallel plates. Williams and Lord [15] studied the flow in circular channels.

There have been several notable solution techniques for the flow inside cavities of complex shape. In one method, the mold geometry is laid flat and then described through a series of simpler geometries: radial flow, flow between parallel plates and flow in circular channels [16, 17]. The finite-element method has been used to simulate the Hele-Shaw flow as applied to injection and compression mold filling [18, 19]. Given the moving boundaries involved, it is necessary to generate a new mesh after each successive time step. The cost and inconvenience of finite element remeshing has led to the use of the boundary element techniques in general cavity flow [20, 21], and the Hele-Shaw flow in particular [22, 23]. While the BEM has obvious advantages over conventional domain methods for the treatment of moving-boundary problems, it suffers from severe drawbacks, the most notable of which is its lack of capability to handle non-linearities such as inertia and non-Newtonian effects, or even a cavity of variable thickness. Hence, the simulation of transient free-surface flows remains challenging since, on the one hand, conventional domain methods are inadequate for adaptive meshing, and, on the other hand, integral methods such as the BEM, which can handle more easily adaptive meshing, cannot incorporate non-linearities from the governing equations.

In the present paper, the difficulties with conventional methods are addressed for the flow inside cavities of general shape but of small thickness. A hybrid Lagrangian/Eulerian method is proposed, which consists of mapping the irregular moving domain, at each time step, onto a fixed rectangular domain. The flow is expanded in Fourier series in the transverse direction, and the finite-difference method is used to obtain the expansion coefficients. The method is used to obtain the three-dimensional flow field inside a thin cavity of arbitrary shape, and a cavity of variable thickness. This corresponds to the solution of a large class of free-surface flow problems, with close relevance to polymer processing. The flow is typically encountered during the filling stage inside a thin cavity as in injection molding. The lubrication assumption is adopted to derive the resultant equations for a Newtonian fluid, averaged over the thickness of the cavity. The influence of the initial domain, and cavity thickness are particularly explored. The cavity is assumed to be symmetric with straight lateral boundaries.

2. GENERAL FORMULATION

In this section, the basic assumptions for the lubrication are first briefly reviewed for viscous fluids. The theory is then extended to include the transient-free-surface flow inside thin three-dimensional cavities.

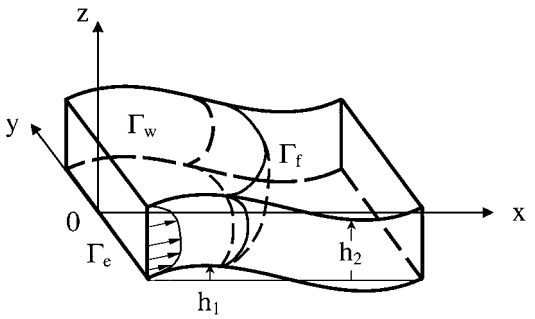

Figure 1. Schematic illustrating the transient free-surface flow inside a cavity induced by the imposed flow at the source boundary, Γ_s.

2.1. General lubrication theory and flow domain

Consider an incompressible Newtonian fluid of viscosity μ. Inertia effects are assumed negligible. The lubrication assumption, which is the hydrodynamic analogue of thin-shell theory, is applied to determine the flow. In most lubrication films the thickness of the film is small compared with its lateral dimensions. Properly handled, this observation can be used to eliminate from the hydrodynamic equations and boundary conditions the dependence upon one of the three spatial variables. The continuity equation is integrated across the film and the Navier–Stokes equation is used to evaluate the quantities appearing as integrands. The conservation equations are formulated in the narrow-gap limit. These equations are first cast in terms of dimensionless variables. Typically, in thin-cavity flow, there are three characteristic lengths. Two length scales, L_1 and L_2, lie along the lateral directions (length and width). A third length scale, H, reflects the order of magnitude of the thickness of the cavity in the depthwise direction. It is usually assumed that L_1 and L_2 are large length scales, of the same order, L, say. In this case, L and H will be taken as the reference length and thickness in the horizontal and depthwise directions, respectively, with (x, y) and z being the corresponding co-ordinates. The velocity components, (u_x, u_y) and u_z are scaled by V and εV, respectively, where V is a reference velocity, and $\varepsilon = H/L$ is the typical aspect ratio in the problem. The time, t, is scaled by L/V, and the pressure, p, is scaled by $\mu V/L\varepsilon^2$. The position vector of a general point in space is denoted by $\mathbf{r}(x, y, z)$, and its projection in the (x, y) plane is denoted by $\mathbf{x}(x, y)$.

Figure 1 illustrates schematically the general flow and notations used. The figure shows a step of the filling stage of a thin cavity of general shape. If terms of $O(\varepsilon^2)$ and higher are excluded, and in the absence of inertia, the conservation equations reduce to the following equation for the pressure [4]:

$$(h^3 p_{,x})_{,x} + (h^3 p_{,y})_{,y} = 0 \tag{1}$$

where $h = h(\mathbf{x})$ is the prescribed dimensionless thickness of the cavity. It is important to observe that the pressure, $p(\mathbf{x}, t)$, does not vary with the depthwise direction. This is in accord with the major hypothesis of lubrication theory. The velocity components are

given by

$$u_\alpha(x,y,z,t)=\frac{p_{,\alpha}(x,y,t)}{2}[z-h_1(x,y)][z-h_2(x,y)],\quad \alpha=x,y \tag{2}$$

where $h_1(\mathbf{x})$ and $h_2(\mathbf{x})$ are the heights of the lower and upper cavity surfaces, respectively (see Figure 1). Note that $h(\mathbf{x})=h_2(\mathbf{x})-h_1(\mathbf{x})$. If the thickness is constant, then the pressure is governed by Laplace's equation. The problem thus reduces to the determination of the scalar variable, $p(\mathbf{x},t)$. This is a quasi-steady problem since the time dependence is not explicit in the pressure equation. The solution will thus be sought in the (x,y) plane. Either the pressure or its normal directional derivative, $q=\mathbf{n}\cdot\nabla p$, is determined, where $\mathbf{n}$ is the normal vector.

2.2. Boundary and initial conditions

Regarding the boundary conditions, the lubrication formulation does not accommodate adherence conditions at the lateral walls. In the reduced momentum equations in the streamwise (x) and spanwise (y) directions, respectively, the diffusive terms $u_{,xx}+u_{,yy}$ and $v_{,xx}+v_{,yy}$ are of $O(\varepsilon^2)$, and are therefore neglected, leading to a reduction in the order of the equations in the x and y directions. However, it is generally accepted that the flow in the core region is not influenced by the boundaries. Stick boundary conditions can only be applied at the bottom and upper rigid cavity surfaces. In this case, only the no-penetration condition applies along the lateral walls. This assumption is not as unrealistic as it seems at first, since the flow core in a thin cavity is not significantly affected by the flow in the immediate vicinity of the lateral walls. However, while this may not be entirely true for a flow at zero Reynolds number, inclusion of inertia makes the problem much more difficult.

The flow is assumed to be driven by an imposed (dimensionless) pressure gradient, $q_0(y,t)$, at $x=0$, so that the general boundary condition at the entrance to the cavity is given by

$$q(x=0,y,t)=q_0(y,t),\quad \mathbf{x}\in\Gamma_e \tag{3}$$

The pressure gradient may be either maintained fixed at all time, or adjusted according to the flow conditions inside the cavity (mold). A time-dependent pressure gradient corresponds typically to the inlet condition in injection molding where the pressure rather than the flow rate is varied with time at the source of fluid. Although a variable pressure gradient can be easily accommodated by the present formulation, q_0 will be assumed to depend only on y. Since the lubrication assumption can only accommodate the no-penetration conditions at the lateral walls, then

$$\mathbf{q}(\mathbf{x},t)=\mathbf{n}(\mathbf{x},t)\cdot\nabla p(\mathbf{x},t)=0,\quad \mathbf{x}\in\Gamma_w(t) \tag{4}$$

where $\mathbf{n}$ is the unit normal to $\Gamma_w(t)$.

At the front (free surface) the imposition of a suitable dynamic condition is not obvious for thin-cavity flow. It is clear that for the general three-dimensional flow, and in the absence of surface tension effects, a zero-traction condition must apply at the front. To leading order, the dynamic condition reduces to the vanishing of the pressure at the free surface [4]:

$$P(\mathbf{x},t)=0,\quad \mathbf{x}\in\Gamma_f(t) \tag{5}$$

Finally, this section is concluded with some remarks on the kinematic condition at the free-surface, which is the least obvious among the boundary conditions to implement. In a

Lagrangian representation, such as the present formulation, the moving boundary is assumed to deform with the fluid velocity, such that the evolution of $\Gamma_f(t)$ is governed by the equation

$$\frac{\mathrm{d}\mathbf{r}}{\mathrm{d}t} = \mathbf{u}(\mathbf{r}, t), \quad \mathbf{r} \in \Gamma_f(t) \tag{6}$$

Although easy to implement, the resulting scheme based on Equation (6) tends to sweep points on the moving boundary along the tangent to the moving boundary, even if only small shape changes take place. Consequently, frequent redistribution of the moving boundary points or remeshing would be necessary if relation (6) is used. Alternatively, the moving boundary can be assumed to deform point wise along the normal with the normal projection of the fluid velocity at the moving boundary. This method keeps the points evenly distributed on the moving boundary. The alternative kinematic boundary condition is obtained by taking the scalar product of Equation (6) with the vector $\mathbf{n}(\mathbf{r}, t)$ to the front, $\Gamma_f(t)$, and noting that $\mathbf{n} \cdot \mathbf{n} = 1$, one has $\mathbf{n} \cdot (\mathrm{d}\mathbf{r}/\mathrm{d}t) = \mathbf{n} \cdot \mathbf{n}(\mathbf{n} \cdot \mathbf{u})$. An equivalent solution of this equation is obtained from the following kinematic condition:

$$\frac{\mathrm{d}\mathbf{r}}{\mathrm{d}t} = \mathbf{n}(\mathbf{r}, t)[\mathbf{u}(\mathbf{r}, t) \cdot \mathbf{n}(\mathbf{r}, t)], \quad \mathbf{r} \in \Gamma_f(t) \tag{7}$$

In this case, the free-surface deforms only in the normal direction. Although condition (7) requires the calculation of the normal vector at the free-surface, no remeshing of the free-surface points is needed in this case since the points remain evenly distributed on the free surface. Remeshing may still be necessary in case of large element distortion. Moreover, condition (7) is particularly advantageous to use in the present context. However, Equation (6) can be more advantageous because of simplicity of implementation. In the current study, the difficulty of node sweeping will be easily circumvented as will be observed below.

3. SOLUTION PROCEDURE

The lubrication problem is solved by first mapping the flow domain onto a rectangular domain. A modified pressure is introduced, which reduces to the pressure when the cavity thickness is constant. The method of Galerkin projection is used, whereby the modified pressure is expanded in Fourier series. The expansion coefficients are then determined by solving the projected pressure equation.

3.1. Domain of computation and reduced problem

The domain of computation is obviously the projection $\Omega_{xy}(t)$ of the physical domain $\Omega(t)$ onto the (x, y) plane. For simplicity, the cavity is assumed to be straight at the entrance, with $x = 0$ and $y \in [-1, +1]$, and the flow is assumed to enter the cavity at a flow rate that depends only on y. Other flow configurations are easily formulated. Thus, at the entrance to the cavity, $q_0(y, t) = -p_{,x}(x = 0, y, t)$, and condition (3) becomes

$$p_{,x}(x = 0, y, t) = -q_0(y, t) \tag{8}$$

At the lateral walls, Equation (4) yields

$$p_{,y}(x, y = -1, t) = p_{,y}(x, y = +1, t) = 0 \tag{9}$$

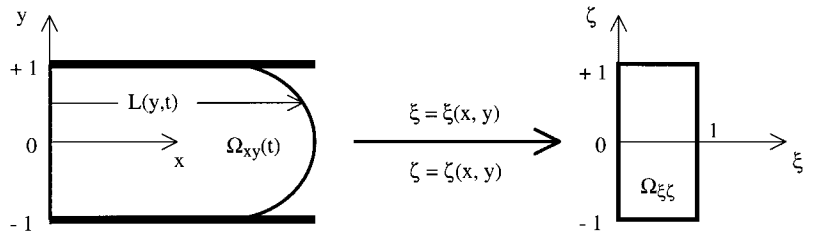

Figure 2. Mapping of the middle slice of the time-dependent physical domain in the (x, y) plane onto the rectangular computational domain in the (ξ, η) plane.

Finally, let the front be represented by $x = X(y,z,t)$, for $z \in [h_1, h_2]$ and $t > 0$. One can then set

$$p(x = X, y, t) = 0 \tag{10}$$

Once $p(\mathbf{x}, t)$ is determined from Equation (1), at a given time, t, the velocity components are then determined. Particularly, the velocity components at the front are required in order to determine the evolution of the front. The following form of the kinematic condition (6) is used in this work:

$$U_x(y,z,t) = X_{,t}(y,z,t) + U_y(y,z,t)X_{,y}(y,z,t) \tag{11}$$

where $U_\alpha(y,z,t) = u_\alpha(x = X, y, z, t)$ are the velocity components at the front. It is important to observe that the z dependence in Equation (11) is implicit, and that X is regarded as dependent on x and y for a given z value (see next).

3.2. Domain mapping

In order to represent the modified pressure, S, in series of orthonormal functions, the domain of computation must be rectangular. For this, the physical domain $(x, y) \in \Omega_{xy}(t)$ is mapped onto the domain $(\xi, \eta) \in [0, 1] \times [-1, 1]$. The mapping is schematically shown in Figure 2. Here $L(y,t) = X(y, z = h_1 + h/2, t)$. More specifically, consider the projection of the flow, at a given time t, in the (x, y) plane. If the width at $x = 0$ is taken as twice the reference length, then $\Omega_{xy}(t) = \{(x, y) \,|\, x \in [0, L], y \in [-1, 1]\}$, and

$$\xi(x, y) = \frac{x}{L(y,t)}, \quad \zeta(x, y) = y \tag{12}$$

Upon use of expressions (12), Equation (1) for the modified pressure reads

$$[1 + (\xi L_{,\zeta})^2] p_{,\xi\xi} + \left[2\xi (L_{,\zeta})^2 - \xi L L_{,\zeta\zeta} + 3 \frac{h_{,\xi}}{h} \right] p_{,\xi} - 2\xi L L_{,\zeta} p_{,\xi\zeta} + L^2 p_{,\zeta\zeta} = 0 \tag{13}$$

subject to the following boundary conditions:

$$p_{,\xi}(\xi = 0, \zeta, t) = a(\zeta^2 - 1) \tag{14}$$

where a is a positive quantity, reflecting the strength of the incoming flow

$$p(\xi=1,\zeta,t)=p,_{\zeta}(\xi,\zeta=-1,t)=p,_{\zeta}(\xi,\zeta=+1,t)=0 \tag{15}$$

The parabolic form for the pressure gradient, given by (14), is chosen somewhat arbitrarily. Other forms are of course easily accommodated by the present formulation. In typical injection molding operations, the pressure is maintained or known (from measurement) at the entrance to the cavity.

The pressure is coupled to the shape of the front, $L(y,t)$, which must be determined as part of the solution, thus making the problem non-linear. The shape of the front in turn delimits the domain in the (x,y) plane. Once $p(x,y,t)$ is obtained at a given time, the horizontal velocity components at the front are evaluated. $L(y,t)$ is then determined by solving the kinematic, which, in the horizontal plane, reduces to

$$U(y,t)=L,_{t}(y,t)+V(y,t)L,_{y}(y,t) \tag{16}$$

where $U(y,t)=U_x(y,z=(h_2-h_1)/2,t)$ and $V(y,t)=U_y(y,z=(h_2-h_1)/2,t)$ are the velocity components at the front in the (x,y) plane, and $L(y,t)=X(y,z=0,t)$.

3.3. Pressure expansion

The modified pressure can be expressed as

$$p(\xi,\zeta,t)=\sum_{n=0}^{\infty} p_n(\xi,t)\cos n\pi\zeta \tag{17}$$

Note that expression (17) satisfies the two lateral boundary conditions (15). If the flow is not symmetric with respect to the x-axis, then odd modes must be included in the pressure expansion. Obviously, a truncation level will have to be imposed, leading to a finite number of modes, N, in the expansion. If expression (17) is substituted into Equation (13), and the Galerkin projection method is used, then the following recursive relation is obtained for the pressure coefficients:

$$\sum_{n=0}^{N} A_{mn}\,p_{n,\xi\xi}+\sum_{n=0}^{N} B_{mn}\,p_{n,\xi}+\sum_{n=0}^{N} C_{mn}\,p_n=0 \tag{18}$$

where $m\in[1,N]$, and the time-dependent coefficient matrices are given by

$$\begin{aligned}
A_{mn}(\xi,t) &= \langle\cos(m\pi\zeta)\cos(n\pi\zeta)[1+(\xi L,_{\zeta})^2]\rangle \\
B_{mn}(\xi,t) &= \left\langle\cos(m\pi\zeta)\left\{\left[2\xi(L,_{\zeta})^2-\xi LL,_{\zeta\zeta}+3\,\frac{h,_{\xi}}{h}\right]\cos(n\pi\zeta)+2n\pi LL,_{\zeta}\sin(n\pi\zeta)\right\}\right\rangle \\
C_{mn}(t) &= -n^2\pi^2\langle L^2\cos(n\pi\zeta)\cos(m\pi\zeta)\rangle
\end{aligned} \tag{19}$$

where the notation $\langle\ \rangle=\int_{-1}^{1}\mathrm{d}\zeta$ is used. In this case, the Galerkin projection consists of multiplying Equation (13) by $\cos(m\pi\zeta)$ for $m\in[1,N]$, and integrating it with respect to ζ from -1 to 1, after substituting expression (17). The boundary conditions for system (18)

are deduced from conditions (14) and (15), leading to

$$p_n(\xi = 1, t) = 0 \tag{20}$$

$$p_{n,\,\xi}(\xi = 0, t) = a\langle(\zeta^2 - 1)\cos(n\pi\zeta)\rangle \tag{21}$$

System (18) is a set of N partial differential equations in ξ and t. However, since time is not explicitly apparent, the system can be regarded as a set of ordinary differential equations in ξ at a given time, t. This is a two-point boundary-value problem. The equations are solved using a variable order, variable step size finite-difference method in ξ, with deferred corrections (IMSL-DBVPFD). Once Equation (18) is solved, $p(\mathbf{x}, t)$ can be determined over the domain $\Omega_{xy}(t)$, in particular along the front $x = L(y, t)$, which in turn allows the determination of the velocity at the front. Similarly to the pressure expansion (17), $L(\zeta, t)$, is expanded as

$$L(\zeta, t) = \sum_{n=0}^{N} L_n(t)\cos n\pi\zeta \tag{22}$$

The Galerkin projection is used to solve Equation (16), and the coefficients $L_n(t)$ are governed by following set of coupled ODEs:

$$\frac{\mathrm{d}L_m(t)}{\mathrm{d}t} = \sum_{n=0}^{N} D_{mn}(t)L_n(t) + E_m(t), \quad m \in [1, N] \tag{23}$$

where the coefficients are given by

$$\begin{aligned} D_{mn}(t) &= n\pi\langle\cos(m\pi\zeta)\sin(n\pi\zeta)V(\zeta, t)\rangle \\ E_m(t) &= \langle\cos(m\pi\zeta)U(\zeta, t)\rangle \end{aligned} \tag{24}$$

A forward explicit finite difference in time is used to solve Equation (23). The numerical assessment of the method is covered in the next section.

4. NUMERICAL ASSESSMENT AND RESULTS

The formulation and solution procedure are now used to examine the transient free-surface flow inside thin cavities of general shape, of constant and variable thickness. Three flow configurations for a cavity of constant thickness are examined, namely, the flow inside a flat cavity with initial rectangular domain, initial parabolic domain, and the flow inside a curved cavity with initial rectangular domain. The influence of cavity thickness is examined for a flat cavity. All results are given in terms of dimensionless quantities. The accuracy of the results is assessed by examining the influence of higher-order modes. The calculations are based on a driving pressure with $a = 1$.

4.1. Flow inside a flat cavity with initial rectangular domain

Consider the flow inside a flat cavity. The length and the width are taken to lie along the x and y directions, respectively, with the x-axis lying halfway between the lateral sides of the cavity (see Figure 2). The thickness of the cavity is assumed to be constant, so that $h_1 = 0$

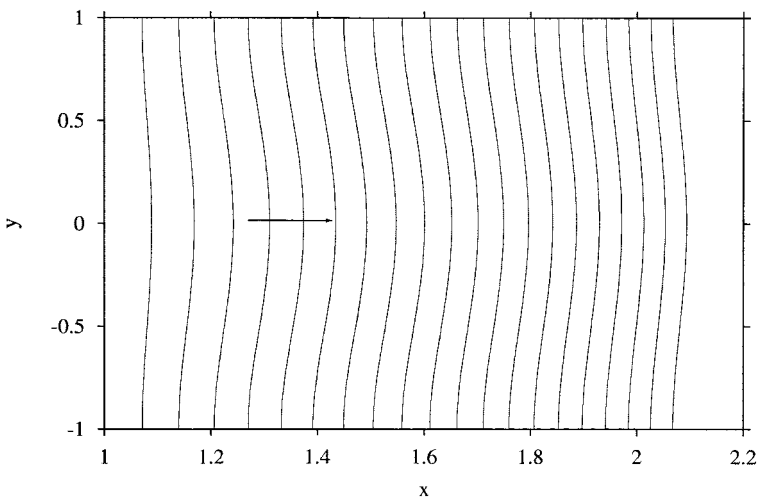

Figure 3. Transient flow inside a flat plate with initial rectangular domain. The fronts are shown at equal time intervals over a period of 20 time units. Results are based on $N=3$. The arrows in this and subsequent figures indicate the direction with time.

and $h_2=1$. Although the fluid is flowing predominantly in the x direction, there is a strong secondary flow in the y direction as well. The first problem considered corresponds to an initial rectangular domain occupied by the fluid. Its projection in the (x, y) plane is given by $\Omega_{xy}(t=0)=\{(x, y)\,|\,x\in[0, 1], y\in[-1, 1]\}$. Figure 3 shows the evolution of the front in the (x, y) plane at $z=0.5$ between the two flat plates. The front is shown at equal intervals over a period of 20 time units, excluding the initial configuration for clarity. The figure indicates that the front remains relatively straight despite the parabolic driving pressure gradient at the entrance $x=0$. It is interesting to observe that the maximum flow at $x=0$ does not induce a relatively strong maximum in the middle of the front. This is the result of the slip of the flow at the lateral boundaries $y=\pm1$. The figure indicates that the spacing between two successive fronts diminishes with time. This is of course expected since a time-independent pressure gradient is imposed at the entrance. The results in Figure 3 are based on only three modes ($N=3$) in the pressure expansion (17). The influence of higher-order modes is negligible as will be concluded next.

A better quantitative assessment is possible by monitoring the time evolution of the front tip, $X_{\max}(t)$, and of the contact point, $X_c(t)$. The convergence of the method has also been examined. Figure 4 displays this evolution of $X_{\max}$ for three truncation levels, namely, $N=1$, 2 and 3. The starting point, at $t=0$, is $X_{\max}=1$ for the front tip, corresponding to the initial fluid domain. Although the increase in $X_{\max}$ is monotonic with time, the rate of the increase diminishes continuously with time. The influence of the higher-order modes is insignificant in this case. In fact, the use of only one mode leads to a reasonably accurate result. Convergence is clearly attained for $N>2$. The results for $N=2$ and 3 are essentially the same. The figure indicates that the one-mode solution tends to underestimate the value of $X_{\max}$. The fast rate of convergence is expected in the present case given the simplicity of the initial domain and subsequent flow. However, the rate of convergence appears to be always high, even for

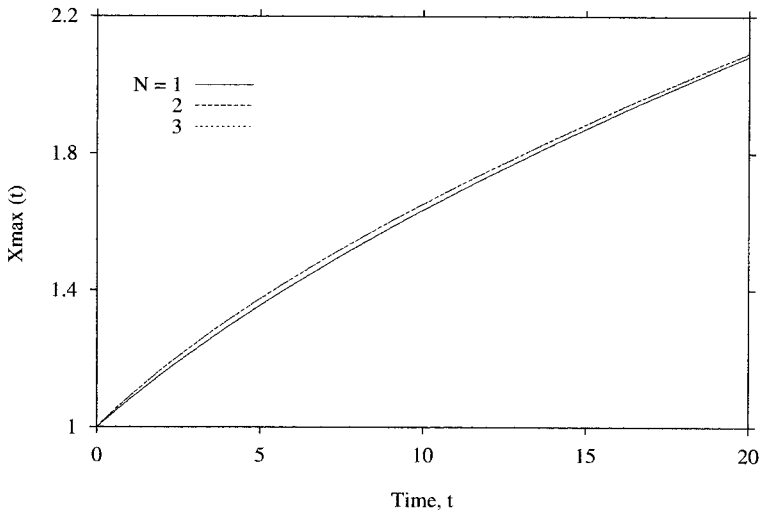

Figure 4. Evolution of the front tip position, X_{max}, with time for the flow inside a flat plate with initial rectangular domain for three levels of truncation, $N = 1,\ 2$ and 3.

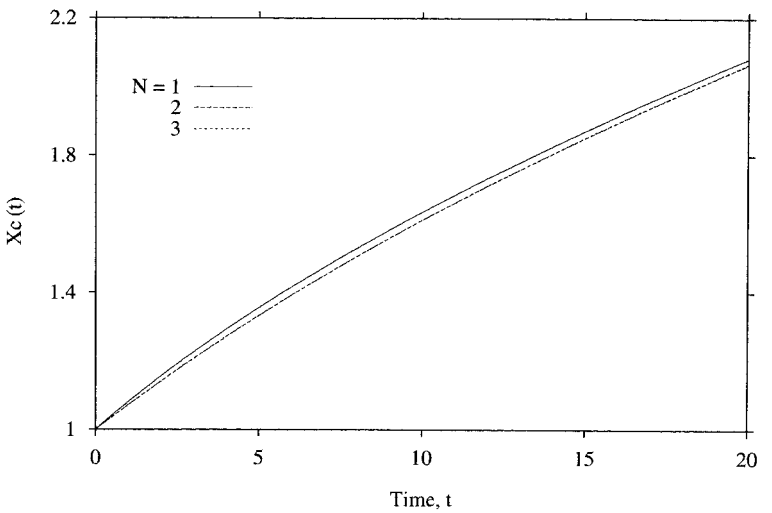

Figure 5. Evolution of the contact point position, X_c, with time for the flow inside a flat plate with initial rectangular domain for three levels of truncation, $N = 1,\ 2$ and 3.

complicated flows as will be seen next. Similar observations are drawn when the evolution of X_c is examined. The results are shown in Figure 5. The figure shows, however, that the one-mode solution tends to overestimate the value of X_c. The two- and three-mode expansions lead to essentially the same results.

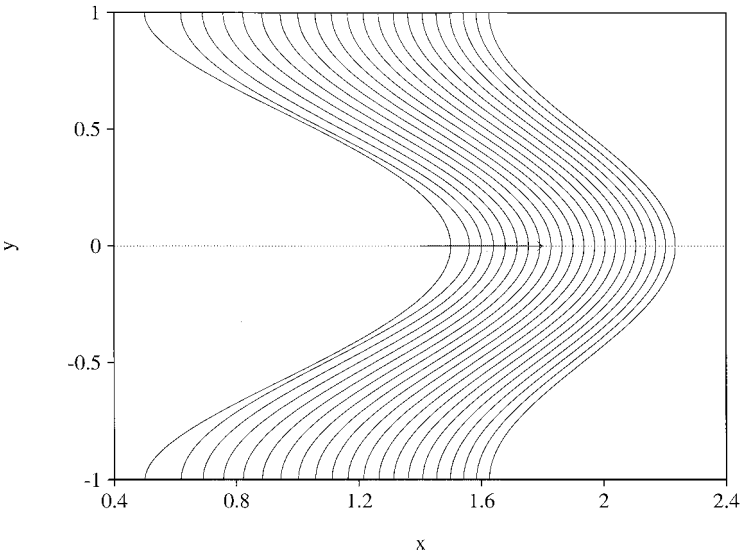

Figure 6. Transient flow inside a flat plate with initial parabolic domain. The fronts are shown at equal time intervals over a period of 20 time units. Results are based on $N=3$.

4.2. *Flow inside a flat cavity with an initial parabolic domain*

Consider now the flow corresponding to the initial parabolic domain given by $\Omega_{xy}(t=0)=\{(x,y)\,|\,x\in[0,0.5-(y-1)(y+1)],y\in[-1,1]\}$, which is subject to the same inlet flow at $x=0$ as above. The sequence of flow fronts is depicted in Figure 6, which shows a relatively dominant axial flow, leading to the straightening of the front with time. Indeed, the fluid in the vicinity of the lateral boundaries tends to flow faster, eventually straightening the front. Note that the initial domain is only partly shown in the figure for clarity. The strength of the lateral flow is assessed in Figure 7, where the flow field is depicted after 0.1 time unit. The fountain flow is clearly reflected in the figure. However, this flow will tend to diminish in intensity with the fluid advancement.

As in Figure 3, the results shown in Figure 6 are based on three modes in the pressure expansion. Convergence is attained at this level of truncation. The rate of convergence is, however, slower in this case given the complexity of the flow. There is a significant discrepancy between the one-mode and higher-mode curves, both quantitatively and qualitatively. For $N=1$, there is a decrease in the rate of advancement of the front tip, similarly to the problem with a rectangular initial domain. The inclusion of higher-order modes, however, indicates that the tip advances at an essentially constant rate. This is depicted in Figure 8 as $X_{\max}$ varies almost linearly with time. The figure also shows the influence of the time increment, Δt. Convergence is attained for $\Delta t<0.1$. The contact point between the front and lateral walls moves at a faster rate initially as shown in Figure 9. The rate of advancement of the contact point, $\mathrm{d}X_{\mathrm{c}}/\mathrm{d}t$, is larger than that of the front tip, $\mathrm{d}X_{\max}/\mathrm{d}t$. This rate of advancement tends, however, to decrease with time, and eventually becomes comparable to $\mathrm{d}X_{\max}/\mathrm{d}t$. This is also indicated in Figure 6, and is reflected by the straightening of the front.

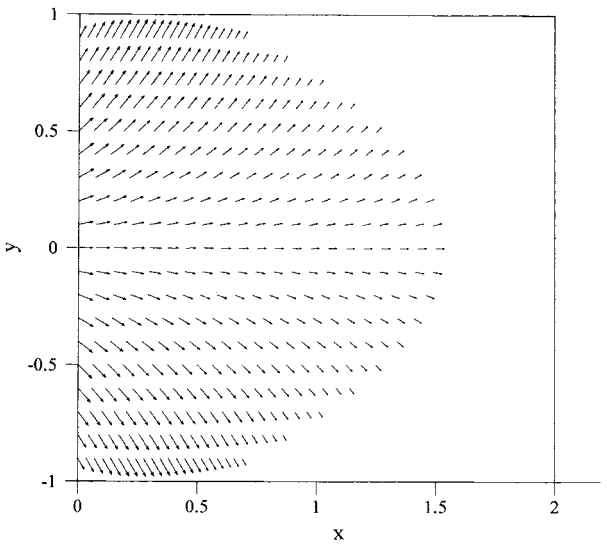

Figure 7. Flow field at $t = 0.1$ for the flow inside a flat plate with initial parabolic domain.

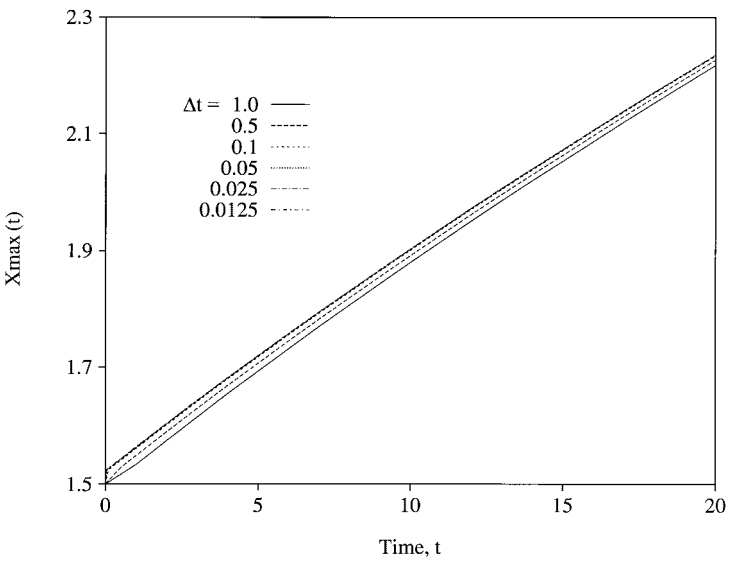

Figure 8. Evolution of the front tip position, $X_{\max}$, with time for the flow inside a flat plate, with initial parabolic domain ($N = 3$). The figure shows the influence of the time increment for the range $\Delta t \in [0.0125, 1]$.

The flow field at the front is further appreciated by examining the velocity vector at the front. Figures 10 and 11 show the distributions of the axial and lateral components at the front, $U(y,t)$ and $V(y,t)$, respectively. The arrow in the figures indicates the time direction. The

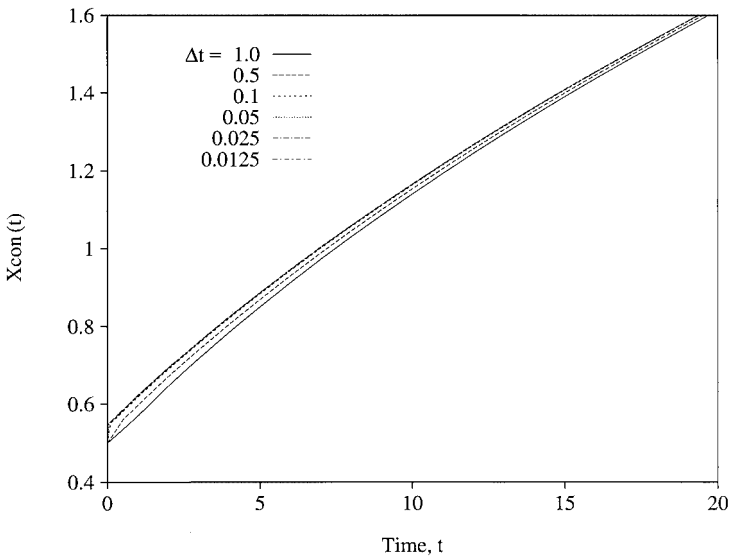

Figure 9. Evolution of the contact point position, X_c, with time for the flow inside a flat plate, with initial parabolic domain, for three levels of truncation ($N=3$). The figure shows the influence of the time increment for the range $\Delta t \in [0.0125, 1]$.

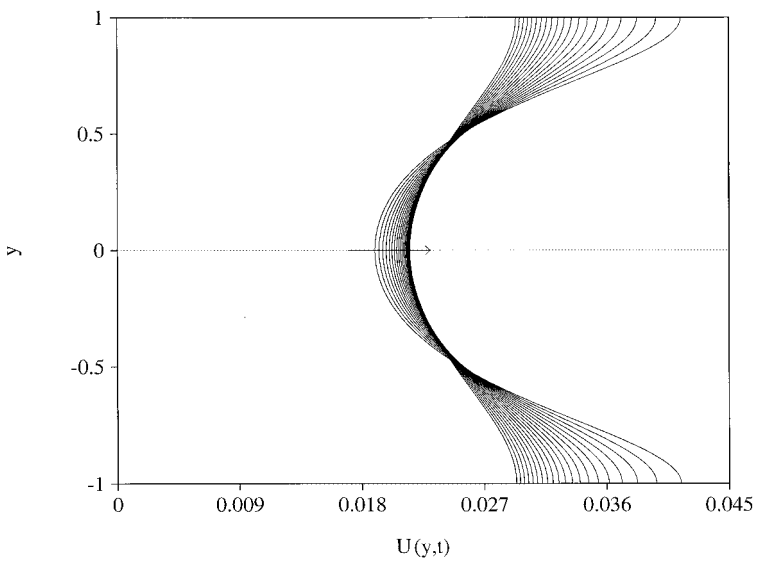

Figure 10. Distribution of the axial velocity component, $U(y,t)$, at the front for $0<t<10$, for the flow in Figure 6.

discrepancy between the velocity of the front tip, $U(0,t)$, and that of the points of contact, $U(\pm 1,t)$, is obvious from Figure 10, which shows that $U(0,t)$ is less than half $U(\pm 1,t)$ in the initial stages. This discrepancy decreases with time. The figure also shows that the velocity

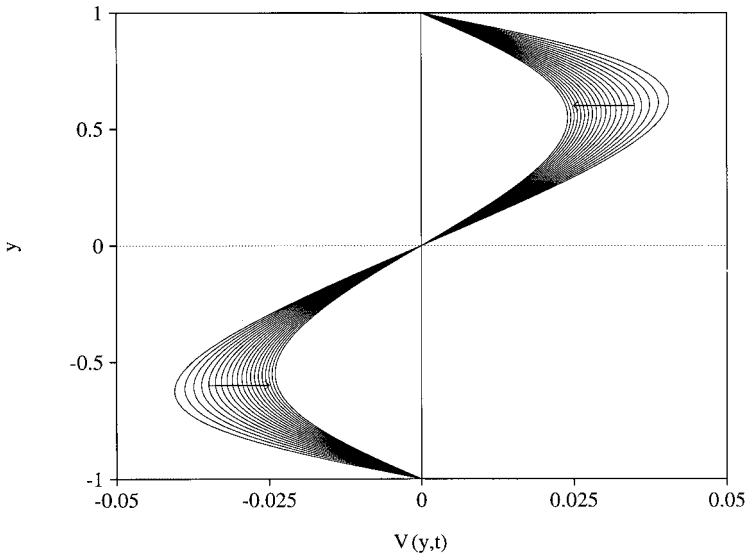

Figure 11. Distribution of the lateral velocity component, $V(y,t)$, at the front for $0<t<10$, for the flow in Figure 6.

tends to generally converge in the long time everywhere except near the lateral walls. The lateral velocity component, $V(y,t)$, is strongest initially, and is generally of the same order of magnitude as $U(y,t)$, as depicted from Figure 11, and is also confirmed in Figure 7. As expected, the lateral velocity vanishes at $y=\pm 1$. The overall non-linear behaviour is further evidenced by examining the plots in the (U,V) plane (not shown here). The plots are closed orbits that are similar to those emerging from dynamical systems. They tend to decrease in the overall diameter, confirming the weakening of the flow with time.

4.3. Transient free-surface flow inside a (3D) curved cavity

The results on the flow inside a flat cavity in Figures 3 and 6 clearly illustrate the strong influence of the initial domain on the ensuing flow sequence. To this must be added the influence of the inlet flow, which can be adjusted to compensate, for instance, the loss of flow near the lateral walls as in Figure 6. However, this adjustment is not needed in this case given the slip at the lateral walls, which allows the flow at the walls to catch up with the flow in the middle region. In this section, the flow in a curved three-dimensional cavity is considered, which illustrates further the intricacies resulting from the influence of the inlet flow, the shape of the initial domain, and the slip at the lateral walls.

So consider the flow inside the curved parabolic cavity whose mid-surface is given by $z=-4(x-1)(x-2)(y-1)(y+1)$, where $(x,y)\in[1,2]\times[-1,1]$. Thus, the maximum in z occurs at the mid-point $(x=1.5, y=0)$ and is equal to 1. The initial domain is taken to have the projection $[0,1]\times[-1,1]$ in the (x,y) plane as in the case of the flow inside the flat plate depicted in Figure 3. The resulting flow sequence is shown in Figure 12 for a period of 20 time units. The scale in the figure indicates the front at six successive and equal intervals. The remarkable feature of the flow is that the fluid at the lateral walls surpassed the fluid in

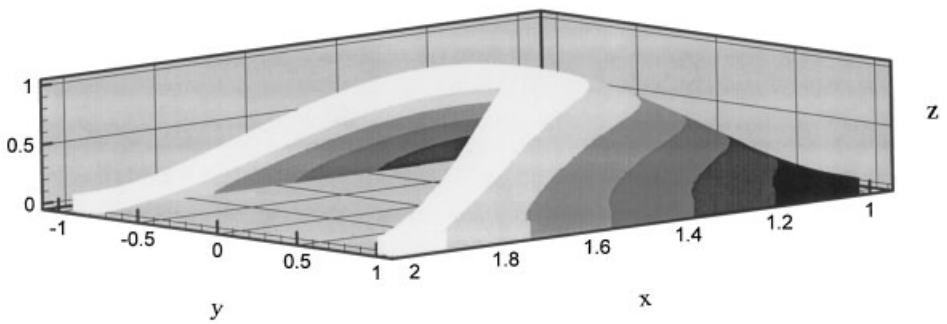

Figure 12. Transient flow inside a curved thin cavity with initial rectangular domain. The fronts are shown at equal time intervals over a period of 20 time units. Results are based on $N=3$.

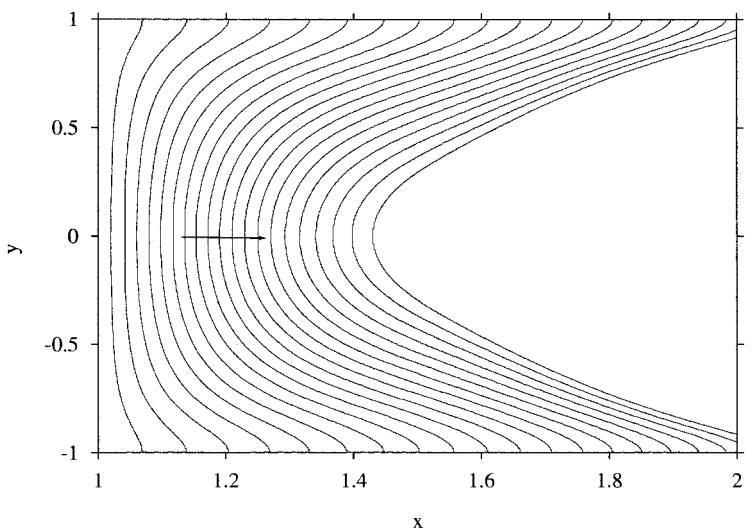

Figure 13. Projection of the fronts of transient flow in Figure 13 in the (x, y) plane.

the rest of the domain, and reached first the corners $(x=2, y=\pm 1, z=0)$. A more accurate assessment is obtained by examining the projection of the fronts onto the (x, y) and (x, z) planes, which are shown in Figures 13 and 14, respectively. The fact that the fluid at the lateral walls surpasses the rest of the fluid is not surprising, since the middle portion of the fluid must cover a larger distance as it climbs up inside the cavity as shown in Figure 14. What is physically less obvious is the extent to which the fluid in the middle region is left behind. The evolution of the front tip along $x, X_{\max}(t)$, the contact point, $X_c(t)$, and the maximum height, $Z_{\max}(t)$, is shown in Figure 15. The results for $X_{\max}$ and X_c should be compared to those in Figures 8 and 9, respectively. It is interesting to observe that the behaviour of $X_{\max}$ is essentially linear with time, similarly to the flow inside a flat cavity (Figure 8). There is even a slight acceleration toward the end of the simulation. The contact point and the maximum

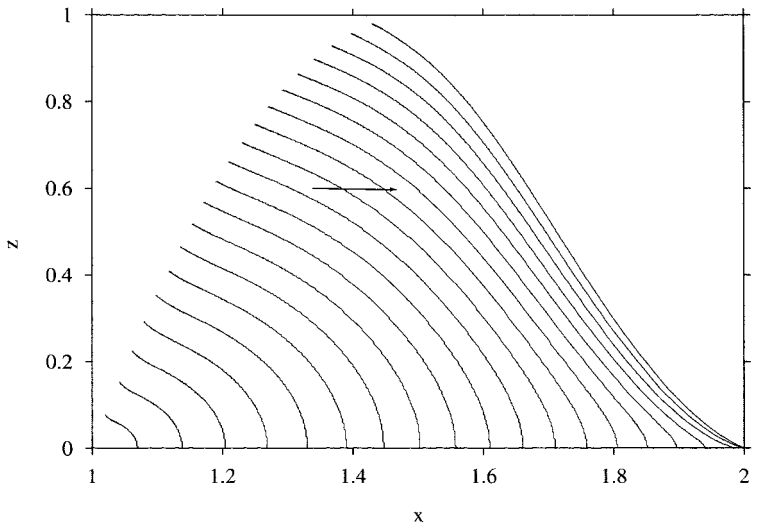

Figure 14. Projection of the fronts of transient flow in Figure 13 in the (x,z) plane.

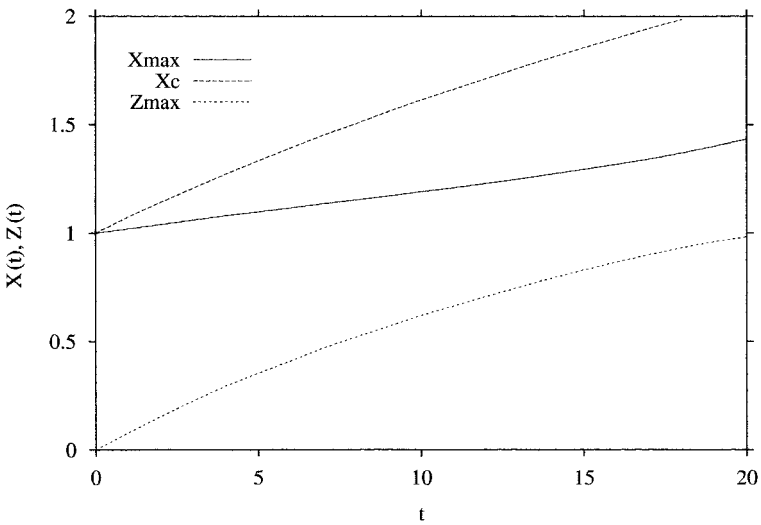

Figure 15. Evolution of the front tip position, $X_{\max}$, the contact point position, X_c, along the lateral walls, and maximum height, $Z_{\max}$, with time for the transient flow problem in Figure 13.

height, on the other hand, tend to accelerate initially, eventually decelerating. Their rate of advance, however, remains higher than that of the front tip.

The flow field at the front is further appreciated by examining the velocity vector at the front. Figures 16 and 17 show the distributions of the axial and lateral velocity components at the fronts of Figure 13, $U(y,t)$ and $V(y,t)$, respectively. The profiles are shown over a period of only 10 period units for clarity. The difference between the velocity of the front tip,

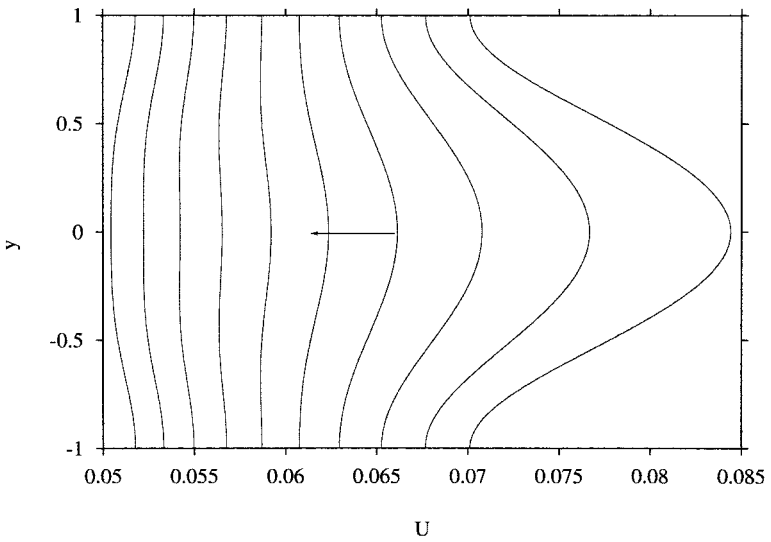

Figure 16. Distribution of the axial velocity component, $U(y,t)$, at the front for $0<t<10$, for the flow in Figure 13.

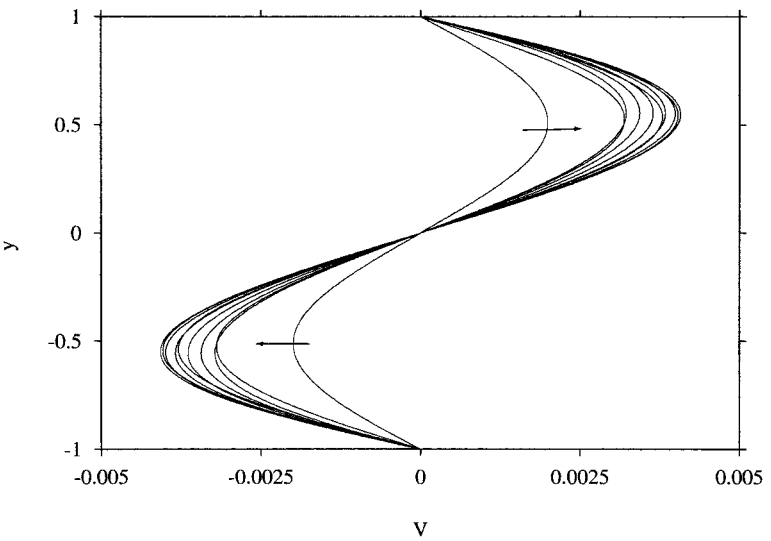

Figure 17. Distribution of the lateral velocity component, $V(y,t)$, at the front for $0<t<10$, for the flow in Figure 13.

$U(0,t)$, and that of the points of contact, $U(\pm 1,t)$, is significant initially, but not as much in Figure 10. This difference not only decreases with time, but the tip eventually begins to recede relative to the lateral walls. Although the velocity tends to generally converge in the long time everywhere, this rate of convergence is much smaller than in Figure 10. Similarly

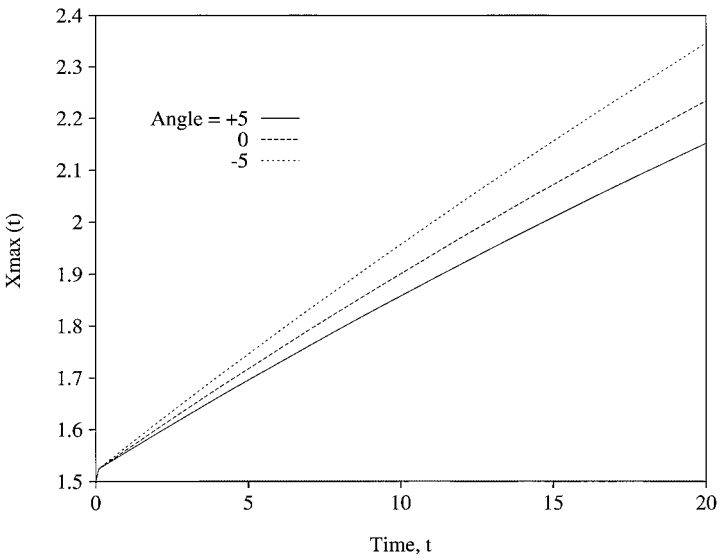

Figure 18. Influence of cavity surface inclination on the evolution of the front tip position, $X_{\max}(t)$. Here α is the angle of inclination (in degrees).

to Figure 11, the lateral velocity component, $V(y,t)$, is strongest initially, but is generally one order of magnitude smaller than $U(y,t)$, as depicted from Figure 17. The (U,V) orbits in the early stages are reminiscent of the limit cycle of a harmonic oscillator. They do not necessarily decrease in their overall diameter as for previously. There is, however, a growing distortion of the orbits, reflecting a growth in non-linearity with time. The orbit width diminishes with time, reaching a minimum, and increasing again. This indicates that the difference $U(0,t)-U(\pm 1,t)$, between the axial velocity at the front tip and the lateral walls, decreases to zero, and then increases again as the velocity at the walls exceeds that at the tip. Simultaneously, the lateral velocity, $V(y,t)$, exhibits an opposite behaviour. Indeed, the lateral flow reaches maximum strength when the axial flow is at its minimum.

4.4. Influence of cavity thickness

So far, all reported results have been restricted to a cavity of constant thickness, $h(\mathbf{x})=1$. In this section, the influence of cavity thickness is examined. This influence can be intricate given its local character. Three types of thickness distributions will be investigated, a linearly diverging, linearly converging, and undulating cavity. Only variation along the x direction will be examined.

Consider first the flow inside a cavity of thickness $h(\mathbf{x})=\tan(\alpha)x+1$, where α is the angle of inclination of the cavity walls. The influence of α on the flow is illustrated in Figure 18, which shows the evolution of the front tip for three values: $\alpha=+5,\ 0$ and -5°, corresponding to a diverging, flat, and converging cavity, respectively. The flow rate is the same for the three configurations. As expected, the figure shows that the flow is weakened by cavity expansion $(\alpha=+5^\circ)$.

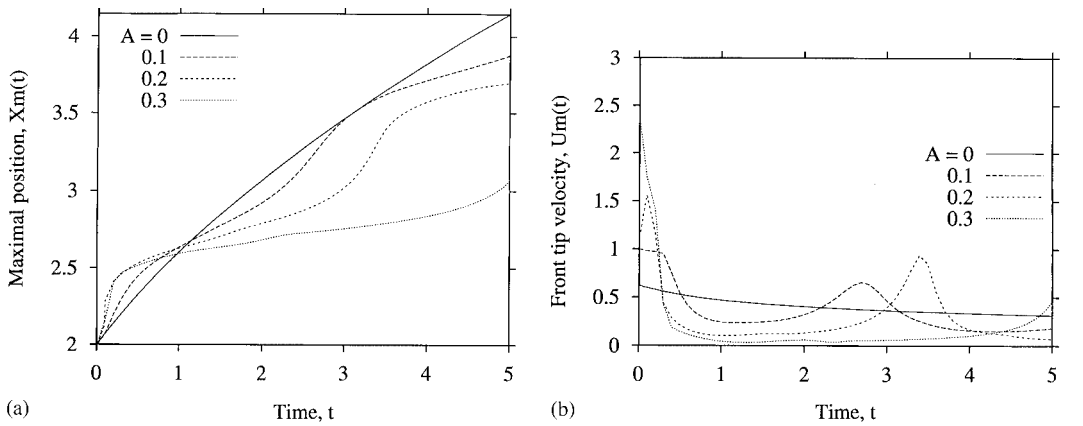

Figure 19. Influence of cavity modulation amplitude, A, on the evolution of the front tip position (a) and velocity (b), for $\omega = 6$.

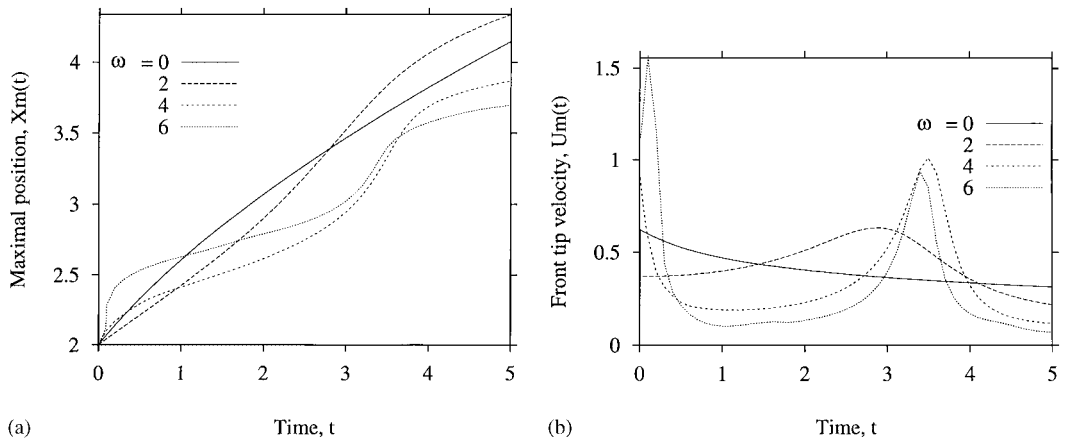

Figure 20. Influence of cavity modulation wavenumber, ω, on the evolution of the front tip position (a) and velocity (b), for $A = 0.2$.

For the flow inside a cavity with wavy walls, the thickness is taken as $h(\mathbf{x}) = 1 + A\sin(\omega x)$, where A is the amplitude and ω is frequency. Figure 19 shows the influence of $A \in [0, 0.3]$ on the evolution of the front tip position, $X_{\max}(t)$, and its velocity $U_{\mathrm{m}}(t)$, for $\omega = 6$. The case $A = 0$ corresponds to a cavity of constant thickness. The figure shows that as A is increased (from zero), the flow behaves in an oscillatory manner with time. There does not seem to be a fixed frequency in the flow response, but the flow appears to fluctuate mostly in the initial stage. It is interesting to observe that the frequency of the flow is affected by the amplitude A. The effect of wall wavenumber is further assessed in Figure 20, which shows the influence of $\omega \in [0, 6]$ for $A = 0.5$. Generally, the front tip moves at the same average rate as for a flow between flat walls. However, there is a sharp drop in rate as ω is increased (from zero), and a gradual regain in the value of $X_{\max}(t)$ as ω increases further.

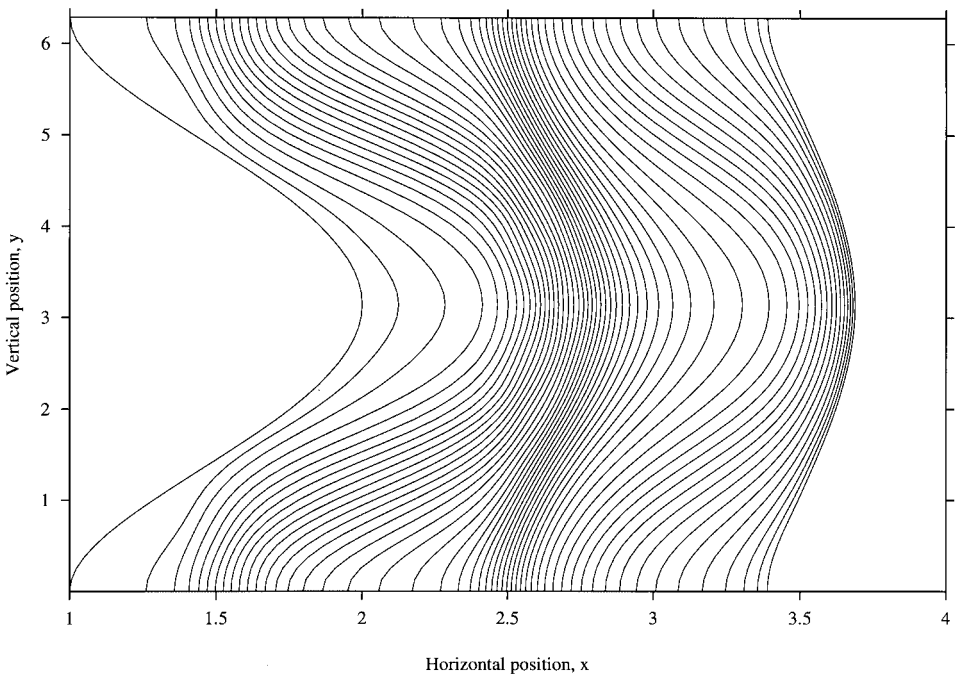

Figure 21. Transient flow inside a modulated cavity ($A = 0.2$ and $\omega = 6$) with initial parabolic domain. The fronts are shown at equal time intervals over a period of 5 time units.

A closer assessment of the influence of cavity modulation on the flow dynamics is carried out for $A = 0.2$ and $\omega = 6$, for a fluid with initial front given by $x = 2 - y^2$. These conditions are typically favourable for the development interesting dynamics as illustrated in Figures 21–23. The evolution of the front is shown in Figure 21, which exhibits a strong spatial modulation with respect to the y direction. The behaviour should be contrasted with that reported in Figure 6. Cavity modulation leads to spatial and temporal modulations in the front shape and location. The modulations become particularly obvious upon examination of the tip and contact points, $X_m(t)$ and $X_c(t)$ in Figure 21. Both points tend to advance monotonically with time as far as their positions are concerned. However, their rate of advancement changes with time depending on whether the fluid is going through a cavity contraction or expansion. The front modulations, however, completely disappear at the later stage. The velocity response is reported at five different time stages, $t \in [1, 5]$. The modulation in flow is quite evident from Figures 22 and 23, where the axial and transverse velocity components at the front are shown, respectively.

5. CONCLUSION

The general lubrication formulation is extended for transient free-surface flow inside a three-dimensional cavity of arbitrary shape and thickness. A low-dimensional spectral approach is proposed to solve the moving-boundary problem. In this work, the irregular and time-

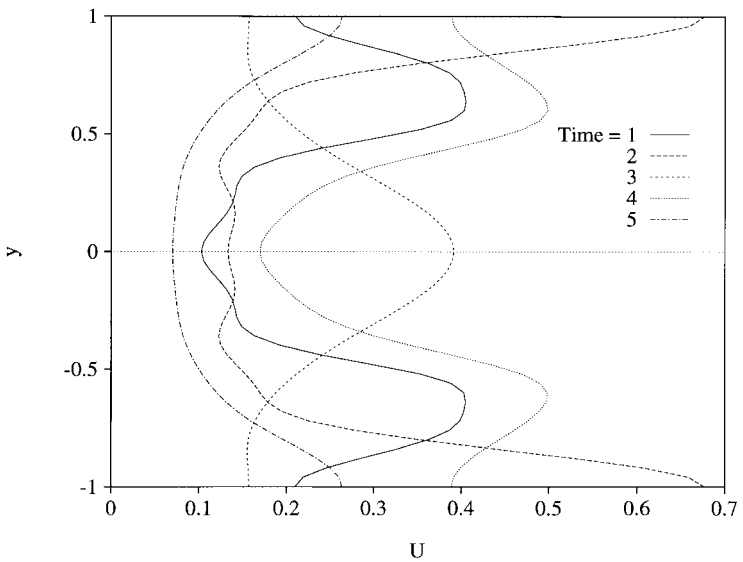

Figure 22. Distribution of the axial velocity component, $U(y,t)$, at the front for $0<t<5$, for the flow in Figure 21.

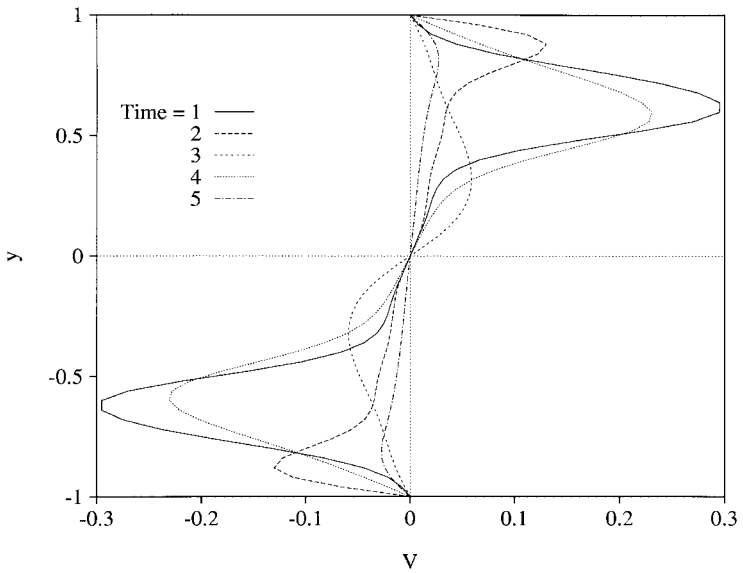

Figure 23. Distribution of the lateral velocity component, $V(y,t)$, at the front for $0<t<5$, for the flow in Figure 21.

dependent domain in the (x, y) plane is mapped onto the fixed rectangular domain $(\xi,\zeta)\in[0,1]\times[-1,1]$. A modified pressure is introduced. The transformed pressure equation is solved by expanding the (modified) pressure in Fourier series along the ζ direction. The expansion

coefficients are determined by solving the projected equations using a multiple-step finite-difference method. It is generally found that only few modes are needed to secure reasonable accuracy and convergence. The validity of such low-dimensional description rests mainly on the fact the front topography is simple in the problems covered in the study. This is, however, expected to be generally true for more complex thin-cavity flows since the front is relatively always simple given the slip of the flow that results from the lubrication hypothesis.

Three transient free-surface flow configurations are examined. In all cases, the driving pressure gradient is parabolic and maintained fixed at the cavity entrance. First, the flow inside a flat plate with the fluid occupying initially a rectangular domain is studied. In this case, the flow in the middle region tends to accelerate initially relative to the flow at the lateral walls. However, the slip at the walls eventually rendered the front straight again, leading to a plug-flow situation in the (x, y) plane. Second, the flow inside the same plate with initial parabolic domain is examined, which exhibits a strong lateral flow initially. This flow, however, diminishes in intensity, leading to the straightening of the front with time. The flow inside a curved cavity (initially rectangular) shows that the fluid tends to advance more rapidly than in the middle region, leaving a significant void in this region. In addition, the flow inside a cavity of variable thickness is examined, for a cavity of linearly varying and undulating thickness. The interplay between spatial and temporal modulations is particularly emphasized in the latter configuration.

ACKNOWLEDGEMENTS

The present work is supported by the Natural Sciences and Engineering Council of Canada.

REFERENCES

1. Hele-Shaw HS. The flow of water. *Nature* 1989; **58**:34.
2. Homsy GM. Viscous fingering in porous media. *Annual Review of Fluid Mechanics* 1987; **19**:271.
3. Park CW, Homsy GM. *Journal of Fluid Mechanics* 1984; **139**:291.
4. Hamrock BJ. *Fundamentals of Fluid Film Lubrication*. McGraw-Hill: NewYork, 1994.
5. Richardson S. Hele-Shaw flows with a free boundary produced by the injection of fluid into a narrow channel. *Journal of Fluid Mechanics* 1972; **56**:609.
6. Agassant JF, Avenas P, Sergent JPh, Carreau PJ. *Polymer Processing*: *Principles and Modeling*. Hanser: Munich, 1991.
7. Tadmor Z, Gogos CG. Principles of Polymer Processing, Wiley: New York, 1979.
8. Middleman S. *Fundamentals of Polymer Processing*. McGraw-Hill: New York, 1977.
9. Kamal MR, Kenig S. The injection molding of thermoplastics. *Polymer Engineering Science* 1972; **12**:294.
10. Winter HH. Approximate calculation and measurement of the pressure distribution in radial flow of molten polymers between parallel discs. *Polymer Engineering Science* 1975; **15**:460.
11. Berger JL, Gogos CG. A numerical simulation of the cavity filling process with PVC in injection molding. *Polymer Engineering Science* 1973; **13**:102.
12. White JL. Fluid Mechanical analysis of injection mold filling. *Polymer Engineering Science* 1975; **15**:44.
13. Broyer E, Gutfinger C, Tadmor Z. *Transactions of the Society of Rheology* 1975; **19**:423.
14. Van Wijngaarden H, Dijksman JF, Wesseling P. *Journal of Non-Newtonian Fluid Mechanics* 1982; **11**:175.
15. Williams G, Lord HA. Mold filling studies for the injection molding of thermoplastic materials. Part I. The flow of plastic materials in hot- and cold-walled circular channels. *Polymer Engineering Science* 1975; **15**:553.
16. Alles H, Philipon S, Agassant JF, Vincent M, Debay G, Lerebours P. *Polymer Engineering Science* 1986; **4**:71.
17. Agassant JF, Alles H, Philipon S, Vincent M. *Polymer Engineering Science* 1988; **28**:477.
18. Hieber CA, Shen SF. A finite-element/finite-difference simulation of the injection molding filling process. *Journal of Non-Newtonian Fluid Mechanics* 1980; **7**:1.
19. Tucker CL, Folgar F. A model compression mold filling. *Polymer Engineering Science* 1981; **23**:59.
20. Khayat RE, Derdouri A, Hebert LP. A boundary-element approach to three-dimensional gas-assisted injection molding. *Journal of Non-Newtonian Fluid Mechanics* 1995; **57**:253.

21. Khayat RE, Derdouri A, Frayce D. Boundary-element analysis of three-dimensional transient mixing processes of Newtonian and viscoelastic fluids. *International Journal for Numerical Methods in Fluids* 1998; **28**:815.
22. Shen SF. Simulation of polymer flows in the injection molding process. *International Journal for Numerical Methods in Fluids* 1984; **4**:171.
23. Barone MR, Oswald TA. Boundary element solution of filed problems. In *Computer Modeling for Polymer Processing. Fundamentals* Tucker III CL (ed.), Hanser: Munich, 1989.

